Arch. Metall. Mater. **68** (2023), 1, 161-170

DOI: https://doi.org/10.24425/amm.2023.141490

FATEMEH KOEINI[1], MAHMOUD HEYDARZADEH SOHI[1*], PARHAM PIRAYESH[2]

SURFACE ALLOYING OF CUPRONICKEL ALLOY WITH ALUMINUM USING TUNGSTEN INERT GAS PROCESS

Surface melting and alloying of Copper-Nickel (Cupronickel) alloy by preplacing aluminum powder and using tungsten inert gas process (TIG) in shielded atmosphere of argon gas were investigated. Surface melting resulted in the formation of a fairly porous dendritic microstructure. Surface alloying with aluminum resulted in the formation of Al_2Cu and Al_4Cu_9 intermetallic compounds along with Cu-rich matrix and unstable martensitic structure. Surface melting reduced the hardness from 140 $HV_{0.1}$ (substrate) to 70 $HV_{0.1}$, mainly due to the loss of cold work effect of the initial substrate. On the other hand, surface alloyed zone showed a hardness of 300 $HV_{0.1}$, mainly due to the formation of intermetallic compound. Tafel polarization results indicated improvement in corrosion resistance of cupronickel alloy after surface melting and alloying.

Keywords: Copper-Nickel; Surface alloying; Surface melting; Aluminum; TIG

1. Introduction

Copper and copper alloys such as cupronickel alloys and aluminum bronze are widely used in marine environments. The natural protective films that form on their surfaces are responsible for their good corrosion resistance in seawater. The two most useful cupronickel alloys are Cu-10Ni and Cu-30Ni [1-3]. Despite superior corrosion resistance and mechanical properties of Cu-30Ni alloys in comparison to Cu-10Ni alloys, the latter is more widely used than the former in marine environments because of its lower price. Presence of both aluminum and nickel in copper alloys (named nickel-aluminum bronze alloys) improve both corrosion and mechanical properties of these alloys in comparison with other copper alloys [4-7]. However, Cu-10Ni alloy may perform poorly under sever corrosive or abrasive conditions.

The amount of the aluminum content nickel-aluminum bronze alloys as well as the cooling rate during solidification can result in the formation of intermetallic phases, Widmanstätten α phase and martensite β' phase which significantly affect ductility, strength and the wear resistance of these alloys. In these alloys, adherent protective layers are formed on their surfaces, in corrosive conditions, which contain both aluminum and copper oxides. Consequently, it is postulated that addition of aluminum to cupronickel alloys should improve the corrosion resistance due to the possible formation of protective aluminum oxide film on the surface of the material [8-11].

liquid surface engineering techniques such as surface melting, alloying and cladding, by applying a number of heat sources like laser and electron beams have been successfully used to enhance the surface properties of copper alloys [12-17].

Zhang et al. [12] found that by using high-current pulsed electron beams (HCPEB), tungsten-surface alloyed layer exhibited increased hardness and corrosion resistance.

In another research Zhang and colleagues [13] noted that chromium-modified copper had a greater potential for improving surface properties than tungsten. Wong et al. [14] employed high power diode laser to form surface layer containing titanium on commercially pure copper and consequently improve corrosion properties. In the case of using titanium as preplaced powder, C.T. Kwok and his co-workers reported that laser surface alloying of commercially pure Cu with titanium at various traveling speeds enhanced hardness and wear resistance due to solid solution strengthening and formation of hard intermetallic phases. It was also noticed that laser-alloyed parts showed better corrosion resistance than commercial copper exposed in synthetic acid rain [15].

Tang et al. [16] enhanced cavitation erosion resistance by laser surface melting of a manganese-nickel-aluminum bronze (MAB). At the other work, they used aluminum powder for surface alloying of propeller bronze. They reported that by increasing the amount of aluminum content in the alloyed layer, corrosion resistance of the material was increased. Laser surface

[1] UNIVERSITY OF TEHRAN, COLLEGE OF ENGINEERING, SCHOOL OF METALLURGY AND MATERIALS ENGINEERING, TEHRAN, IRAN
[2] ISLAMIC AZAD UNIVERSITY, FACULTY OF ENGINEERING, DEPARTMENT OF METALLURGY AND MATERIALS, KARAJ BRANCH, KARAJ, IRAN

* Corresponding author: mhsohi@ut.ac.ir

© 2023. The Author(s). This is an open-access article distributed under the terms of the Creative Commons Attribution-NonCommercial License (CC BY-NC 4.0, https://creativecommons.org/licenses/by-nc/4.0/deed.en which permits the use, redistribution of the material in any medium or format, transforming and building upon the material, provided that the article is properly cited, the use is noncommercial, and no modifications or adaptations are made.

alloying of MAB with Al in comparison to laser surface melting (LSM), led to higher increase in both the corrosion and cavitation erosion resistance in 3.5% NaCl solution [17,18].

Even though, the majority of the liquid phase surface treatments have used laser beams as heat source, tungsten inert gas (TIG) or gas tungsten arc welding (GTAW) is also an interesting alternative. This process is widely used for welding and joining of metals and alloys [19-21]. In contrast to other heat sources such as lasers and electron beams, it is cheaper, easier and more accessible. Moreover, it does not have the problem of low beam absorption by copper alloys in lasers or the limitation of specimen dimensions in the electron beam method [22]. In addition, the resulting surface layer in TIG is thicker than in the laser process [23].

Several studies have been conducted regarding the surface modification of copper alloys and the effects of variables like the traveling speed, the amount of heat input, the materials and types of preplaced powder on the properties of the surface layers.

Raju et al. used GTAW for surface alloying of aluminum bronze electroplated with Cr at various heat inputs. Their study demonstrated the formation of intermetallic phases, and it was also observed that wear and corrosion resistance were improved in the saline environment (3.5 wt.% NaCl) in particular for specimen with higher heat input [24].

Nair et al. surface alloyed Al bronze with nickel using GTAW process [7]. They reported that rapid solidification of the surface layer refined the structure. Furthermore, the hardness of the alloyed zone increased by thickening the pre-placed Ni powder.

Based on the aforementioned studies, it appears that surface modifications could have significant impacts on the tribological and corrosion behaviors of copper alloys. In the present work, surface melting and alloying of Cu-10% Ni alloy were performed via pre-placing aluminum powder and using TIG process as a heat source. The microstructure, hardness and corrosion properties of the material before and after surface melting and alloying were then studied.

2. Experimental

2.1. Materials

The chemical composition (values are in wt.%) of the cupronickel alloy given in TABLE 1 was determined by optical emission spectroscopy (quantometery method). The dimensions of the specimens were 80×50×6 mm. Prior to the surface melting and alloying, the surfaces of the specimens were grinded by emery paper up to 2000 and subsequently cleaned with acetone. For surface alloying, Al powder (>99.9%) with the size distribution under 45 μm was mixed with polyvinyl alcohol as binder and applied on the surfaces of the specimens in the form of a paste. The thickness of preplaced paste was around 0.8-1 mm.

TABLE 1

Chemical composition of Cu-10Ni

Element	Cu	Ni	Fe	Zn	Pb	Sn	Mn	Co
Wt.%	87.71	10.60	0.93	0.60	0.06	0.05	0.04	0.01

2.2. TIG surface process

The surfaces of the bare and preplaced specimens were then melted using a TIG (model Merkle TIG 200 AC/DC) heat source at direct current electrode negative (DCEN) polarity condition. The arc voltage was kept at a constant value of 15 V during surface treatment. A non-consumable 2% thorium oxide tungsten electrode with a diameter of 2.4 mm was used and the distance from the substrate was kept at 1.5 mm to produce a stable arc for all experiments. Surface treatment was carried out using high-purity (99.99%) argon gas with various flow rates of 8, 12, and 16 l/min. TABLE 2 shows the process parameters that have been optimized after several single tracks to achieve a crack-free surface. To code specimens, SM and SA were used for surface melting and surface alloying respectively, followed by the applied currents, travel speed and gas flow rate. Re-melting was experienced on a number of surface alloyed specimens in order to achieve more homogenized structure in the alloyed zone. The heat input for each test was calculated using Eq. (1) [25,26]:

$$\text{Heat input}\ (\text{kJ/mm}) = \frac{(0.48 \times \text{current}(\text{I}) \times \text{voltage}(\text{V}))}{\text{travel speed}\ (\vartheta)} \quad (1)$$

TABLE 2

The operation parameter of TIG surface process

Treatment code	Type of surface treatment	Current (A)	Travel speed (mm/min)	Heat input (kJ/mm)	Flow rate (l/min)	Number of pass
SM150-70	Surface melting	150	70	0.92	8-12-16	1
SM120-40	Surface melting	120	40	1.30	8	1
SM135-40	Surface melting	135	40	1.46	8	1
SA105-30-1	Surface alloying	105	30	1.51	8	1
SA125-30-1	Surface alloying	125	30	1.80	8	1
SA130-30-1	Surface alloying	130	30	1.87	8	1
SA-135-30-2	Surface alloying	135	30	1.94	8	2

2.3. Characterization of surfaced melted and alloyed zone

The treated specimens were cut, then their cross-sections were grinded with emery papers (100-2500) and finally polished with alumina colloid (with the size of 0.05 µm). Cross-sectioned specimens were etched by a solution containing 5 g $FeCl_3$, 50 ml HCl and 100 ml H_2O for metallographic and microstructural examinations. Microstructures of the treated zones were analyzed using optical microscope (Gippon, GDCE-30, Japan), scanning electron microscope (cam-scan MV2300) equipped with energy dispersive spectrograph (EDS) and X-ray diffractometer (Xpert pro, Phillips, Holland). The depths of the treated zones were measured using OLYSIA M3 image analyzer software. Micro-hardness of the treated zones was measured by Leitz Vickers hardness machine at an applied load of 100 gf and a loading time of 15 sec.

2.4. Potentiodynamic polarization tests

Potentiodynamic polarization test was carried out to evaluate corrosion resistance of the original and surface treated specimens. The polarization tests were carried out in a three-electrode cell in 3.5% NaCl solution at room temperature using an EG&G potentiostat/galvanostat, model 273A. Platinum plate and saturated calomel electrode (SCE) were used as counter and reference electrodes respectively. The potentiodynamic polarization test was carried out by sweeping the potential at a scan rate of 2 mVs^{-1}. In order to identify the corrosion products, the corroded surfaces of the specimens were studied by SEM.

3. Results and discussion

3.1. Microstructural analysis

Fig. 1a & b show Cross-sectional views of the surface melted cupronickel alloy achieved at two different flow rates, indicating formation of dendritic microstructures in the melted zones. A number of porosities are seen in these zones. The concentration of these porosities on the top regions of the melted zone are higher than those of the bottom regions. This alloy is prone to absorb oxygen and hydrogen gasses during welding that results in the formation of porosity. During surface melting, the molten pool is inevitably exposed to the atmosphere and Cu-Ni alloys tend to absorb gases from the atmosphere, even if it is shielded by an inert gas like argon during TIG surface melting process. Moreover, the presence of nickel in the Cu-Ni alloys increases the tendency to gas absorption of copper alloys from the atmosphere in liquid state [27,28].

Increasing of heat input showed no significant effect on the amount and size of the porosities. However, when the flow rate of shielding gas increased for better protection of the melted zone from contaminants (Fig. 1a-b), the amount and size of the porosities were extremely reduced. In addition, the depth of the melted zone meaningfully decreased from 3082 µm (8 l/min) and 2173 µm (12 l/min) to 1622 µm (16 l/min) by rising flow rate. Higher flow rate results in lower arc efficiency factor (η), lower heat input due to an increase in heat loss, and hence a smaller melt depth [25,29].

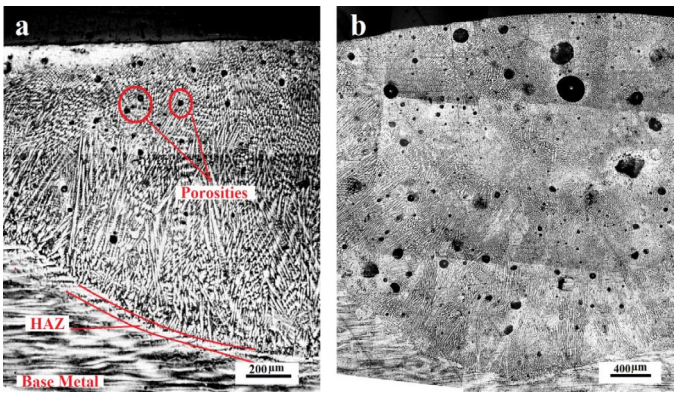

Fig. 1. Cross sectional optical micrographs of the surface melted Cu-Ni zones achieved at two different flow rates. a) SM150-70-16, b) SM150-70-8

Optical micrograph of the aluminum surface alloyed specimen achieved at a heat input of 1.51 kJ/mm (SA105-30-1) is shown in Fig. 2a. As can be seen in this figure, the porosities are completely eliminated and the microstructure involves dendritic structure in the alloyed region. Aluminum tends to react with oxygen and therefore it prevents the formation of gas porosities in the surface treated zone [30]. The XRD pattern in Fig. 2b confirms the presence of a single phase, α solid solution formed

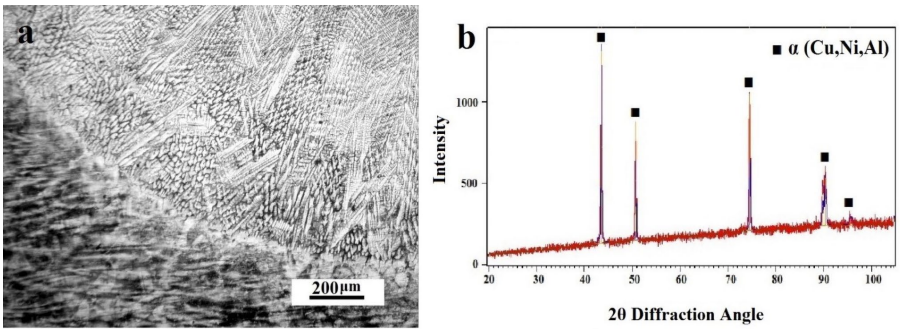

Fig. 2. a) Microstructure, and b) XRD pattern of a surface alloyed specimen (SA105-30-1)

after solidification of the alloyed region. According to X-ray diffraction pattern and microstructural images, it seems that the aluminum content of the alloyed zones obtained at heat input lower than 1.8 kJ/mm is not enough to form intermetallic phases [31].

At higher heat input, the amount of aluminum in the alloyed zone increased and a complex microstructure was formed. Fig. 3a-d show the cross-sectional optical micrographs of the surface alloyed specimen (SA125-30-1). Fig. 3b reveals that the top region of alloyed zone is mainly composed of Al_2Cu (θ) and Al-Cu eutectic structure. Near the interface, the proportion of the eutectic structure is reduced, and replaced by Al_2Cu, as reported by Zhu et al. in their research [32].

According to Cu-Al phase diagram [33], the Al_2Cu (θ) phase can be found in Al content of more than 45 wt. %. Fig. 4 displays typical EDS line profiles for nickel, copper and aluminum obtained from SA125-30-1 specimen showing concentration of different elements in alloyed zone. As can be seen the intensity of aluminum as alloying element is extremely increased in the alloyed zone. Increasing of the amount of Al in the alloyed zone results in the formation of intermetallic phases as well as the enhancement of the hardness [34].

X-ray diffraction patterns of the alloyed zone achieved at a heat input of 1.87 kJ/mm is shown in Fig. 5, confirming the presence of Al_2Cu (θ) and Cu_9Al_4 (γ_2) phases in the alloyed zone, due to the addition of aluminum. The necessary heat to form Al_2Cu intermetallic compound from chemical reaction (-6.1 kJ·mol^{-1}) and its activation energy for the growth (60.66 kJ·mol^{-1}) are lower than those needed for the formation of Cu_9Al_4 (-4.1 kJ·mol^{-1} and 75.61 kJ·mol^{-1}, respectively), which means that the Al_2Cu phase is likely to be formed first and then Cu_9Al_4 will be formed in Cu-rich zone with diffusion of Cu atoms into the Al_2Cu. The growth of this intermetallic compound (Cu_9Al_4) can be increased because of the rising temperature and as a result the diffusion rate. In addition, these consequences support the claim that kinetic factors play more important roles in comparison with thermodynamic factors to form intermetallic compounds [35].

Fig. 3c shows that the microstructure in the middle of the alloyed zone is mainly fine Widmanstätten α. Cooling rate affects the type of β transformation products. Widmanstätten morphology forms at moderate cooling rates from the beta phase which is predominantly seen in nickel-aluminum bronze alloy.

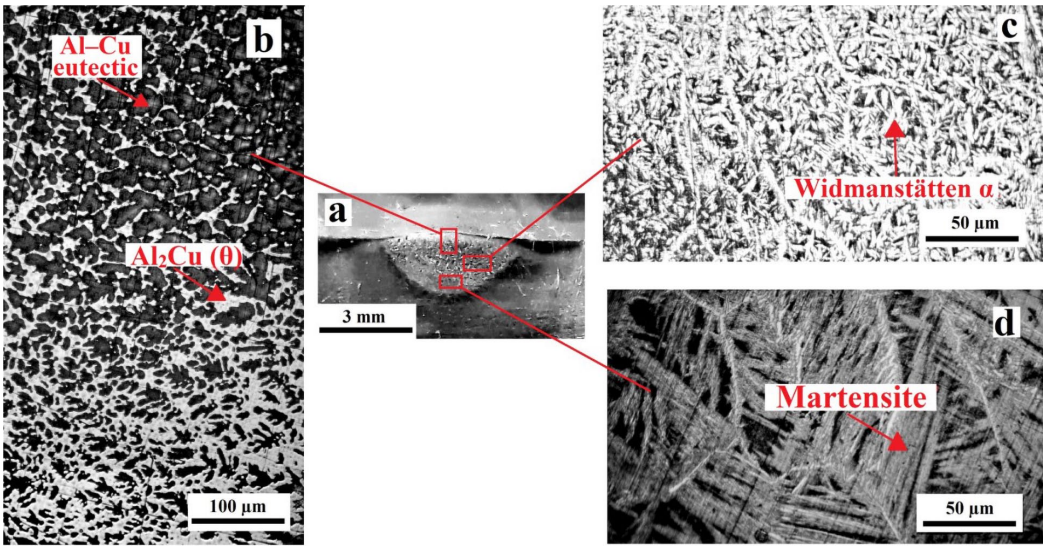

Fig. 3. OM images of the TIG surface alloyed specimen (SA125-30-1). a) cross-section, b) α-Al solid solutions and Al_2Cu (θ) phases, c) Widmanstätten α morphology, and d) Martensitic structure β'

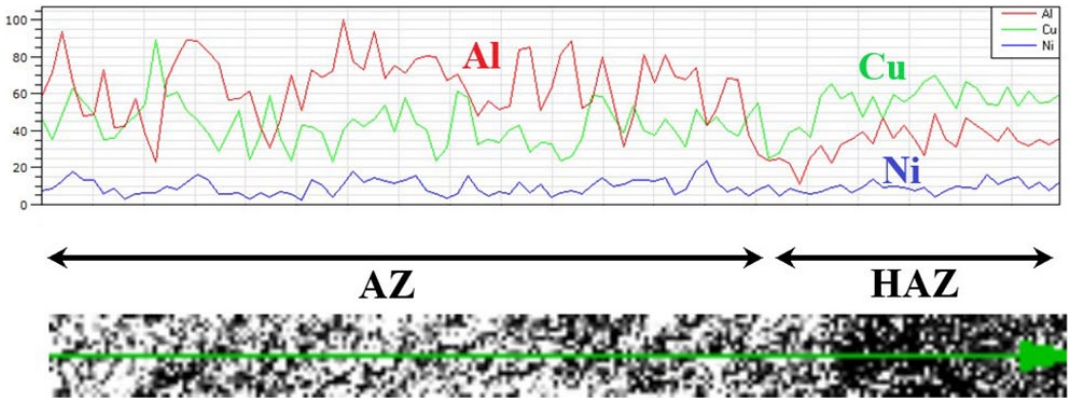

Fig. 4. Line scanning analysis from substrate to the alloyed zone of SA125-30-1 specimen

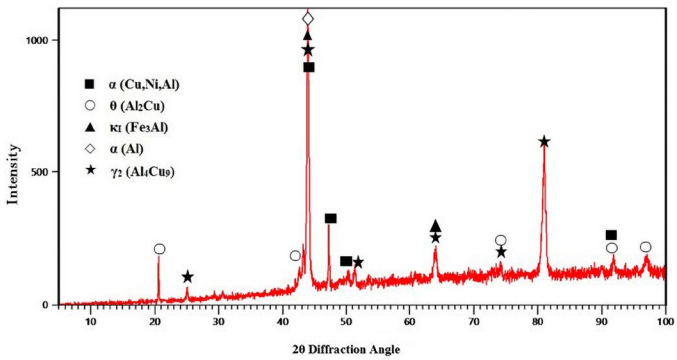

Fig. 5. XRD pattern of the surface alloyed specimen (SA130-30-1) achieved by 1.87 kJ/mm heat input

On the other hand, rapid cooling of aluminum bronze alloys from β-solid solution (bcc) prevents eutectoid transformation and leads to formation of (β') martensitic constituent (β'' β') with a needle-like structure [36-38] as shown in Fig. 3d.

Combining both Ni and Fe with aluminum in nickel-aluminum bronze alloys results in the formation of a number of intermetallic phases, designated as κ, that are obtained at low cooling rate and identified according to their morphologies. As the alloy cools, the beta phase transforms to alpha, kappa phases, and small amount of retained β. The κ_I phase is iron-rich, having a Fe_3Al composition and this phase often have a globular or rosette shaped [39,40]. The microstructure of κ_I phase formed in the alloyed region is shown in Fig. 6a. Fig. 6b reveals that above Widmanstätten zone indeed contains a uniform distribution of spherical Al,Ni-rich precipitates in the α-Cu solid solution, and the results of the EDS analysis are given in TABLE 3. This kind of structure was also observed in the laser surface alloying of copper with Ti and Cr, including the Ti-rich and Cr-rich precipitates, respectively [15,41].

Fig. 7a displays the microstructure of SA135-30-2 specimen that was re-melted by 1.94 kJ/mm heat input after surface alloy-

TABLE 3

The weight and atomic percentage analysis of matrix and precipitates of SA130-30-1 specimen

	Precipitates		Matrix	
	Wt.%	At.%	Wt.%	At.%
Cu	46.8	33.7	67.8	53.8
Al	26.0	45.8	18.3	34.2
Ni	26.2	20.5	13.9	12.0

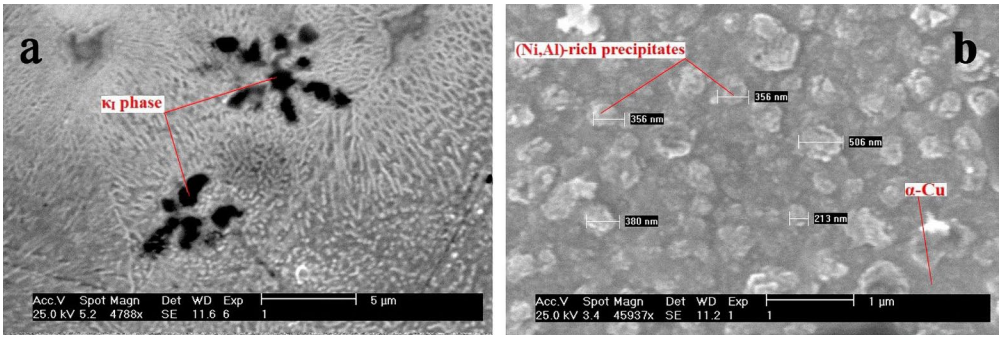

Fig. 6. SEM micrographs showing a) κ_I intermetallic phase formed and uniform distribution, b) of Al-rich precipitates in the alloyed zone of SA130-30-1 specimen

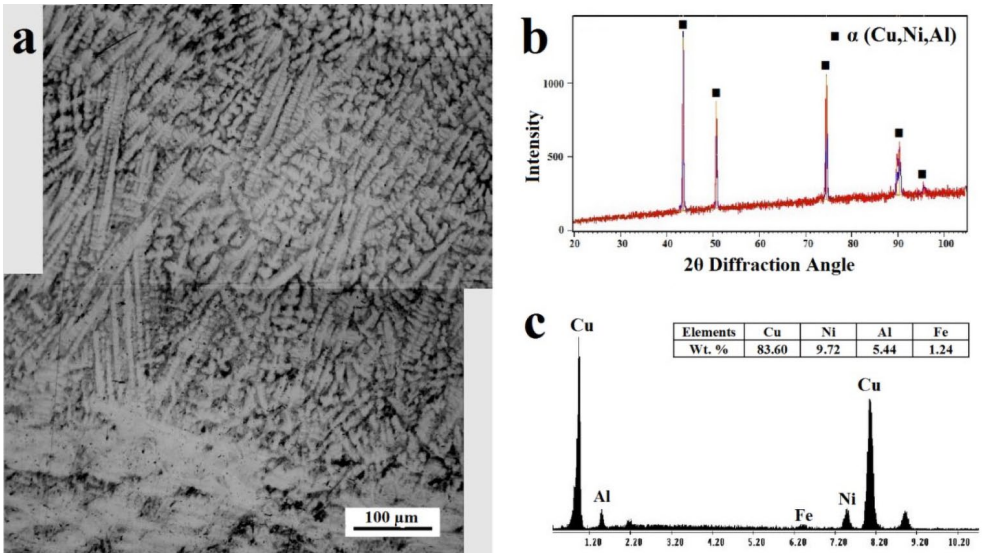

Fig. 7. OM image of surface alloyed specimen achieved at a heat input of 1.94 kJ/mm (SA135-30-2). a) XRD pattern, b) point EDS analysis, c) of alloyed zone

ing and involves dendritic microstructure without any porosity and crack. The EDS analysis and XRD pattern (Fig. 7b, 7c) show the existence of Al in the re-melted zone. Furthermore, the obtained chemical mapping data of elements including Cu, Ni and Al from the alloyed zone is shown in Fig. 8. As can be seen from Fig. 8e, information provided by mapping overlay analysis displays that re-melting was sufficient to melt all intermetallic phases.

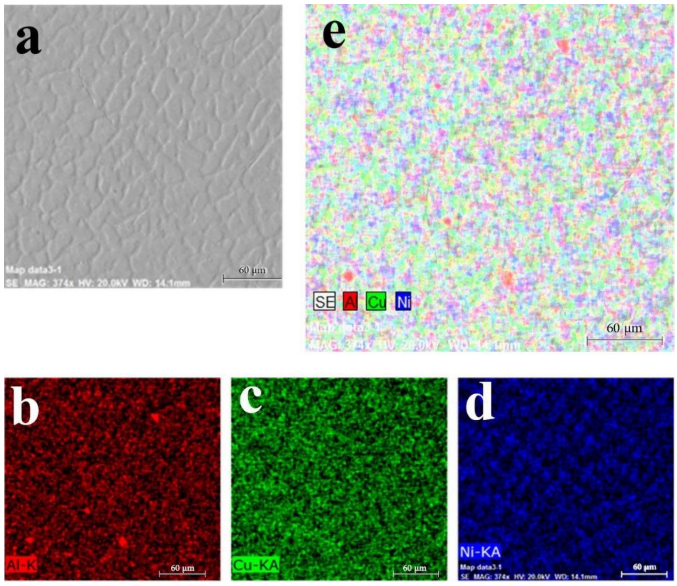

Fig. 8. EDS elemental mapping for SA135-30-2 specimen. a) reference area of analysis, b) Al mapping, c) Cu mapping, d) Ni mapping, e) and Al, Cu and Ni elemental mapping overlay

3.2. Hardness

Fig. 9 compares the microhardness of the melted zone, fusion boundary and HAZ in various surface melted specimens achieved at different heat inputs. The hardness of the untreated specimen was about 140 $HV_{0.1}$. Hardness in the vicinity of the melted zone reduced, because the effect of the work hardening that had been happened during rolling in the fabrication process of the cupronickel alloy is removed by the heat generated during surface melting. As for the melted zone, even though a fairly fine dendritic structure formed in this area, porosities and omission of cold working during surface melting led to the hardness reduction. Meanwhile porosity can cause stress concentration and affect the mechanical properties of the material [42]. The hardness of the melted zone and HAZ of the specimens reduced by increasing the heat input. Reduction of the heat input resulted in the smaller melted zone, but at the same time, higher the cooling rate and formation of finer structure and consequently, higher hardness [19,25,43].

The microhardness profiles of the surface alloyed specimens achieved at different heat inputs and number of melting passes are shown in Fig. 10. In the specimen that was alloyed under heat input lower than 1.8 kJ/mm (SA105-30), the hardness was decreased gradually from near 150 $HV_{0.1}$ in upper region of the alloyed zone to 70 $HV_{0.1}$ in HAZ which is mainly related to the variation of the amount of aluminum in the alloyed zone. The highest hardness value was achieved in specimens alloyed under a heat input higher than 1.8 kJ/mm. In this cases, depth of the alloyed zone was also increased, but at the same time the solubility of the Al in the alloyed zone was also increased. As mentioned before, the presence of the aluminum in the alloyed zone is resulted in the formation of aluminum containing intermetallic phases, that are responsible for the enhancement of the hardness values in these areas [25,44]. The hardness of SA125-30 and SA130-30 specimens reached to values of about 300 and 250 $HV_{0.1}$ respectively, and then decreased gradually toward the base hardness value. A sudden small increase in the hardness was occurred near the interface that might be related to the martensitic and widmanstätten structures formed in these regions due to the high cooling rates at the interfaces [37].

Re-melting of the surface alloyed specimen (SA135-30-2) resulted in dilution of aluminum in the alloyed zone. Thus, the hardness of this specimen was lower than of the single pass treated specimens. Relatively constant hardness values in the alloyed region could be related to the somehow uniform distribution of aluminum in the alloyed zone.

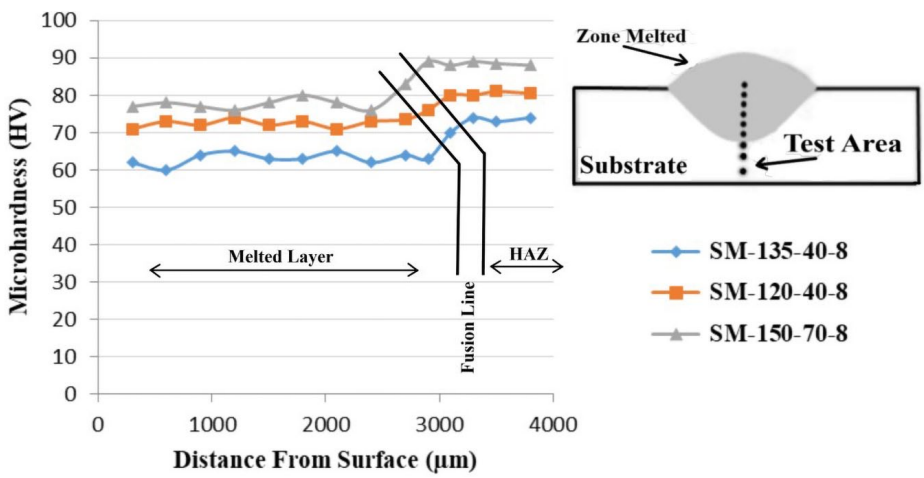

Fig. 9. Hardness profiles of the surface melted (SM) specimens

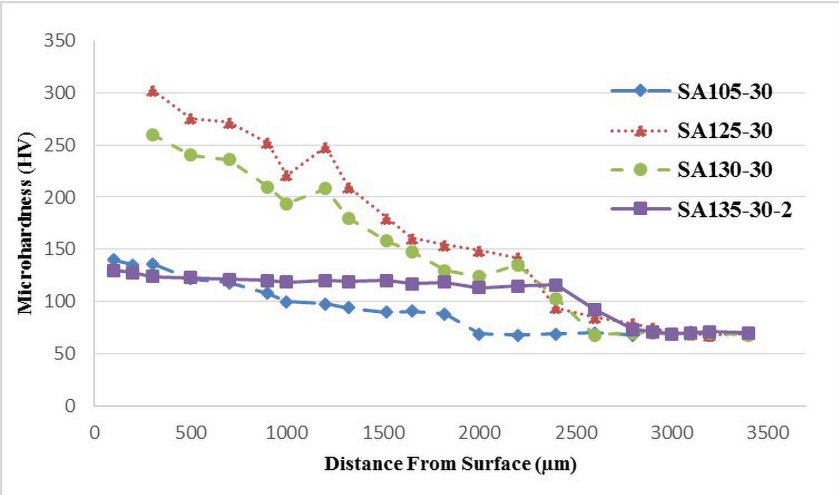

Fig. 10. Hardness profiles of the surface alloyed specimens: SA105-30 (1.51 kJ/mm), SA125-30 (1.80 kJ/mm), SA130-30 (1.87 kJ/mm) and SA135-30-2 (1.94 kJ/mm)

3.3. Corrosion behavior

Corrosion behavior of the substrate, surface melted and alloyed specimens were investigated by Tafel polarization test in 3.5 wt.% NaCl solution. The polarization Tafel curves are shown in Fig. 11. TABLE 4 also reveals some important details that can be achieved from these curves. As it can be seen in anodic region, by further increase of the applied potentials, a strong decrease in the corrosion current of all specimens were observed, that is caused by passivation. This potential is known as primary passivation potential that are about 171 and 55 mV for the substrate and surface melted specimens, respectively. Corrosion products formed (passive layer) on copper-nickel alloys in marine atmosphere and clean seawater usually involve complex mixture of cuprous oxide, often containing nickel and iron oxide, copper hydroxide, copper hydroxychloride and cupric oxide [45]. These

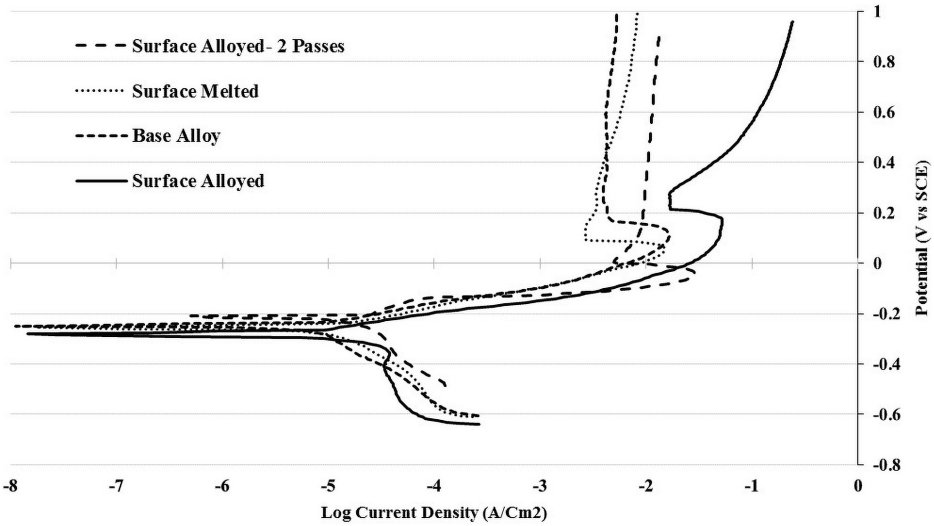

Fig. 11. Tafel polarization curves of base alloy, surface melted and surface alloyed specimens as 1 and 2 pass in 3.5 wt.% NaCl solution

TABLE 4

The details achieved from Tafel polarization curve

	Corrosion current density, i_{corr} ($\mu A/cm^2$)	Corrosion potential, E_{corr} (mV)	Critical current density, i_c (mA/cm2)	Primary passive potential, E_{pp} (mV)	Passive current density, i_p (mA/cm2)	Passive potential, E_{pa} (mV)
Base alloy	7.1878	–249	16.51	171	4.77	171
Surface Melted (SM135-40)	11.3998	–255	14.96	55	2.66	112
Surface Alloyed (SA125-30-1)	3.8361	–281	51.73	175	16.81	215
Surface Alloyed (SA135-30-2)	17.7623	–211	29.28	–45	4.96	5

insoluble films cover the surface of the specimens corroded and prevent ionic transport. In this manner, the adherent surface film enhances corrosion resistance. However, in anodic region, by increasing potential, corrosion current variations in substrate is more stable than surface melted specimen. This instability in behavior of the protective layer formed on the surface melted zone, in higher potential, can be related to presence of porosities on its surface. These porosities can deteriorate the situation of the protective layer and accelerate the corrosion rate due to the increasing of the interface between the specimen and the corrosion solution [46,47]. SEM image of the surface melted specimen is shown in Fig. 12 that in addition to a dense and compact layer of corrosion products on the surface of melted specimen, some porosities in the passive film were formed.

Fig. 12 also indicates the polarization test data of the surface alloying specimens SA125-30-1 and SA135-30-2 in 3.5 wt.% NaCl solution. As it is obvious, sudden decrease in corrosion current for the specimen with one and two-pass alloying was started at 175 and –45 mv, respectively and consequently, the passive layer was formed earlier on the surface of specimen with two-pass alloying. Adherent surface film of the two-pass surface alloyed specimen was formed in lower potential in comparison to another specimen. According to Fig. 11, by increasing potential in anodic region, the variation of corrosion current of two-pass surface alloyed specimen was approximately remained steady and at the top of the curve, it had an ideal situation. It could be inferred from the curve that the passive layer was stable in a wide range of potentials. Whereas, in one-pass surface alloyed specimen, after formation of passive layer, corrosion current was meaningfully changed by the rising of corrosion potential, this means that the protective layer was unstable and can be related to presence of intermetallic phases. Fig. 13a reveals SEM image of one-pass surface alloyed specimen exposed to 3.5 wt.% NaCl solution during polarization test. The protective layer was not uniform and many porosities can be seen on its surface. EDS analysis from the passive film confirm the presence of oxide and chloride compounds in this layer (Fig. 13b).

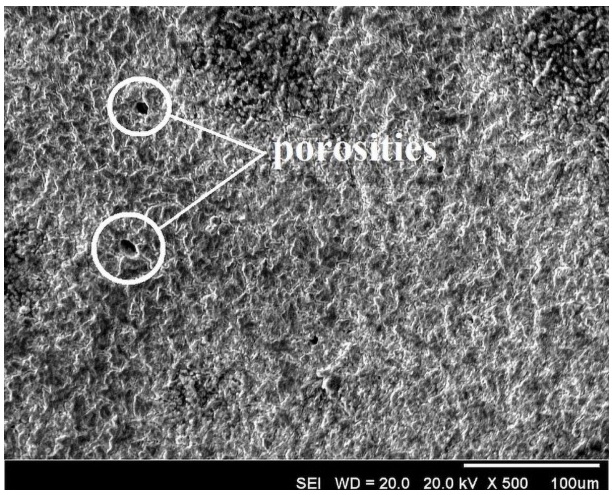

Fig. 12. SEM image of surface of the surface melted specimen (SM135-40) in 3.5 wt.% NaCl solution

According to the TABLE 4, corrosion potential of two-pass surface alloyed specimen is higher than one-pass specimen and consequently, it is more noble than one-pass specimen. On the other hand, corrosion current density of two-pass specimen is also higher than one-pass. This can be attributed to faster formation of protective layer in two-pass specimen, which consisted of aluminum and copper oxides. The corrosion resistance of Cu-Ni alloys depends on the formation of a stable oxide layer on the surface caused by the added alloying element. The protective film on the surface of Ni-Al-bronze (NAB) alloys that contains copper and aluminum oxides (mainly Cu_2O and Al_2O_3) and is improved due to the presence of nickel and iron in this film, increases the corrosion resistance of this alloys when they are exposed in salt solution [6,8,48]. Al-rich oxide layer is adjacent to the substrate and Cu-rich is formed in outer region [49]. In alloys with Al content less than 8 wt. %, the microstructure of aluminum bronze is monophasic and consists of α By increasing the Al content, intermetallic compounds (IMCs) are formed throughout structure, such as Al_4Cu_9 (γ) and κ phases that increase the number of potential sites for galvanic coupling and as a result, reduce the corrosion resistance of these alloys when

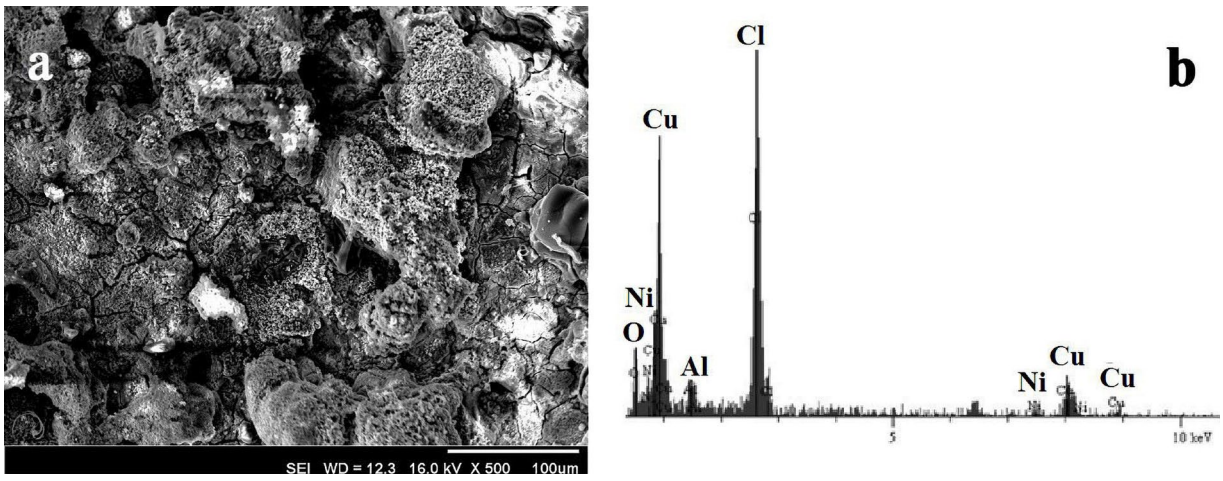

Fig. 13. SEM micrograph of corroded surface. a) and EDS analysis of one-pass surface, b) alloyed specimen (SA125-30-1) in 3.5 wt.% NaCl solution

are exposed to the corrosive environment [47,50,51]. Based on the evidences achieved, in seawater, rapid selective phase and general corrosion can be occurred in aluminum bronzes and nickel-aluminum bronzes[50,52-54].

4. Conclusions

In this study, TIG surface melting and alloying of copper-nickel alloy were performed by pre-placing aluminum powder on the surface before melting. The following results were achieved:

1) The surface melted zones contained porosities. Increasing of the shielding gas flow rate reduced the porosities of the surface melted zones and the depth of the melted zone.
2) In the surface melted zones, although the microstructure became finer, due to the porosities and the loss of the effect of cold work, the microhardness became lower than that of the substrate.
3) Re-melting of the surface alloyed specimen resulted in a homogeneous microstructure without porosity and improvement in microhardness.
4) Microhardness of the specimens that were alloyed at higher heat input reached near maximum of 300 $HV_{0.1}$ as compared to 140 $HV_{0.1}$ for the substrate. The enhancement in microhardness is attributed to the presence of Cu_9Al_4, Al_2Cu intermetallics, α phase with widmanstätten morphology, martensite structure and solid solution hardening.
5) Passive layers were formed on the surfaces of the melted and alloyed specimens and enhanced corrosion resistance.
6) In the two-pass surface alloyed specimen the protective film was formed in lower potential in comparison to another specimens. In the one-pass alloyed specimen, protective layer was unstable due to the presence of intermetallic phases in the specimen structure.

REFERENCES

[1] R. Francis, The Corrosion of Copper and Its Alloys: A Practical Guide for Engineers, NACE International, US. (2010).

[2] X. Zhu, T. Lei, Corros. Sci. **44**, 67-79 (2002).

[3] A.L. Ma, S.L. Jiang, Y.G. Zheng, W. Ke, Corros. Sci. **91**, 245-261 (2015).

[4] Q. Luo, Z. Qin, Z. Wu, B. Shen, L. Liu, W. Hu, Corros. Sci. **138**, 8-19 (2018).

[5] F. Yang, H. Kang, E. Guo, R. Li, Z. Chen, Y. Zeng, T. Wang, Corros. Sci. **139**, 333-345 (2018).

[6] A. Schüssler, H.E. Exner, Corros. Sci. **34**, 1793-1802 (1993).

[7] S. Nair, R. Sellamuthu, R. Saravanan, Effect of Nickel content on hardness and wear rate of surface modified cast aluminum bronze alloy, in: Mater. Today Proc., Elsevier Ltd, 6617-6625 (2018).

[8] Z. Wu, Y.F. Cheng, L. Liu, W. Lv, W. Hu, Corros. Sci. **98**, 260-270 (2015).

[9] A.R.J.S. Murthy, H.N.A. L., S.K. H., Adv. Mater. Process. Technol. (2020). DOI: https://doi.org/10.1080/2374068X.2020.1855403

[10] M.A. Shaik, K.H. Syed, B.R. Golla, Corros. Sci. **153**, 249-257 (2019).

[11] M.D. Fuller, S. Swaminathan, A.P. Zhilyaev, T.R. McNelley, Mater. Sci. Eng. A. **463**, 128-137 (2007).

[12] C. Zhang, P. Lv, J. Cai, C.T. Peng, Y. Jin, Q. Guan, Appl. Surf. Sci. **422**, 582-590 (2017).

[13] C. Zhang, N. Tian, L. Li, Z. Yang, P. Lv, J. Yunxue, H. Zhu, Q. Guan, Vacuum **174**, 109222 (2020).

[14] P.K. Wong, C.T. Kwok, H.C. Man, F.T. Cheng, Corros. Sci. **57**, 228-240 (2012).

[15] C.T. Kwok, P.K. Wong, H.C. Man, Surf. Coatings Technol. **297**, 58-73 (2016).

[16] C.H. Tang, F.T. Cheng, H.C. Man, Surf. Coatings Technol. **182**, 300-307 (2004).

[17] C.H. Tang, F.T. Cheng, H.C. Man, Surf. Coatings Technol. **200**, 2602-2609 (2006).

[18] C.H. Tang, F.T. Cheng, H.C. Man, Surf. Coatings Technol. **200**, 2594-2601 (2006).

[19] G. Rogalski, A. Świerczyńska, M. Landowski, D. Fydrych, Metals **10** (5), 559 (2020).
DOI: https://doi.org/10.3390/met10050559

[20] J. Tomków, K. Sobota, S. Krajewski, Facta Univ. Ser. Mech. Eng. **18**, 611-621 (2020).
DOI: https://doi.org/10.22190/FUME200520044T

[21] J. Górka, M. Przybyła, M. Szmul, A. Chudzio, D. Ładak, Adv. Mater. Sci. **19** (3), 55-64 (2019).
DOI: https://doi.org/10.2478/adms-2019-0017

[22] S.A. Kumar, P. Sathiya, Mater. Manuf. Process. **30** 1154-1159 (2015).

[23] M. Heydarzadeh Sohi, S.M.H. Hojjatzadeh, A. Khodayar, A. Amadeh, Surf. Coatings Technol. **325**, 617-626 (2017).

[24] D. Raju, A.R. Govindan, J. Subramanian, S. Ramachandran, S. Nair, Surface alloying of aluminium bronze with chromium: Processing, testing, and characterization, in: Mater. Today Proc., Elsevier Ltd, 2191-2199 (2019).

[25] A. Ardeshiri, M.H. Sohi, A. Safaei, Surf. Coatings Technol. **310**, 87-92 (2017).

[26] J.H. Park, Y.H. Kim, H.J. Baek, S.M. Cho, J. Manuf. Process. **40**, 140-148 (2019).

[27] L. Brown, Cost-Effective Manufacturing: Joining of Copper and Copper Alloys, CDA. Publ. (98) (1994).

[28] S. Dadras, M.J. Torkamany, J. Sabbaghzadeh, Opt. Lasers Eng. **46**, 769-776 (2008).

[29] F.H. Ley, S.W. Campbell, A.M. Galloway, N.A. McPherson, Int. J. Adv. Manuf. Technol. **80**, 1213-1221(2015).

[30] D.L. Olson, T.A. Siewert, S. Liu, G.R. Edwards, ASM Handbook, Vol. 6 Welding, Brazing, and Soldering, ASM International, Metals Park, Ohio (1993).

[31] W.K. Hamoudi, R.A. Ismail, F.I. Sultan, S. Jaleel, Lasers Manuf. Mater. Process. **4**, 24-35 (2017).

[32] D. Zuo, S. Hu, J. Shen, Z. Xue, Mater. Des. **58**, 357-362 (2014).

[33] E.B. Hannech, N. Lamoudi, N. Benslim, B. Makhloufi, Surf. Rev. Lett. **10** (4), 677-683 (2003).

[34] B. Çorlu, M. Ürgen, Surf. Coatings Technol. **205**, 540-544 (2010).

[35] H. Xu, C. Liu, V.V. Silberschmidt, S.S. Pramana, T.J. White, Z. Chen, V.L. Acoff, Acta Mater. **59**, 5661-5673 (2011).

[36] F.A. Anene, N.E. Nwankwo, V.U. Nwoke, Metall. Mater. Eng. **25**, 147-162 (2019).

[37] J. Fang, G. Song, W. Liu, Q. Li, Microstructure evolution of as-cast nickel aluminum bronze under electropulsing, in: Key Eng. Mater., Trans Tech Publications Ltd, 28-34 (2020).

[38] H.K. Chandra Mohan, S. Devaraj, K.S. Narayana Swamy, Metallogr. Microstruct. Anal. **10**, 36-45 (2021).

[39] T. Murray, S. Thomas, Y. Wu, W. Neil, C. Hutchinson, Addit. Manuf. **33**, 101122 (2020).

[40] Z. Qin, Q. Zhang, Q. Luo, Z. Wu, B. Shen, L. Liu, W. Hu, Corros. Sci. **139**, 255-266 (2018).

[41] J. Dutta Majumdar, I. Manna, Mater. Sci. Eng. A. **268**, 216-226 (1999). DOI: https://doi.org/10.1016/s0921-5093(99)00112-4

[42] A. Morales, O. Piamba, J. Olaya, Coatings. **9** (11), 722 (2019). DOI: https://doi.org/10.3390/coatings9110722

[43] W.G. Jiru, M.R. Sankar, U.S. Dixit, J. Mater. Eng. Perform. **25**, 1172-1181 (2016).

[44] M. Scendo, S. Spadlo, K. Staszewska-Samson, P. Mlynarczyk, Metals **10** (7), 966 (2020). DOI: https://doi.org/10.3390/met10070966

[45] X. Zhao, Y. Qi, J. Wang, Z. Zhang, J. Zhu, L. Quan, D. He, Materials **13** (7), 1790 (2020). DOI: https://doi.org/10.3390/ma13071790

[46] X. Zhao, Y. Qi, J. Wang, T. Peng, Z. Zhang, K. Li, Metals **10** (9), 1227 (2020). DOI: https://doi.org/10.3390/met10091227

[47] D.R. Ni, B.L. Xiao, Z.Y. Ma, Y.X. Qiao, Y.G. Zheng, Corros. Sci. **52**, 1610-1617 (2010). DOI: https://doi.org/10.1016/j.corsci.2010.02.026

[48] Z. Qin, D.H. Xia, Y. Zhang, Z. Wu, L. Liu, Y. Lv, Y. Liu, W. Hu, Corros. Sci. **174**, 108744 (2020).

[49] J.A. Wharton, K.R. Stokes, Electrochim. Acta. **53**, 2463-2473 (2008).

[50] B. Sabbaghzadeh, R. Parvizi, A. Davoodi, M.H. Moayed, Mater. Des. **58**, 346-356 (2014).

[51] D. Liu, H. Chen, J. Wu, E. Then, Corrosion Behavior of Cu-Al Intermetallic Compounds in Copper Wire Bonding in Chloride-Containing Accelerated Humidity Testing, in: Proc. – Electron. Components Technol. Conf., Institute of Electrical and Electronics Engineers Inc. 629-636 (2016).

[52] Q.N. Song, Y.G. Zheng, D.R. Ni, Z.Y. Ma, Corrosion **71**, 606-614 (2015).

[53] R.M. Pidaparti, B.S. Aghazadeh, A. Whitfield, A.S. Rao, G.P. Mercier, Corros. Sci. **52**, 3661-3666 (2010).

[54] A. Al-Hashem, W. Riad, Mater. Charact. **48**, 37-41 (2002).